

BD–22°3467, a DAO-type star exciting the nebula Abell 35 ★ ★★

M. Ziegler¹, T. Rauch¹, K. Werner¹, J. Köppen², and J. W. Kruk³

¹ Institute for Astronomy and Astrophysics, Kepler Center for Astro and Particle Physics, Eberhard Karls University, Sand 1, 72076 Tübingen, Germany,
e-mail: rauch@astro.uni-tuebingen.de

² Observatoire Astronomique de Strasbourg, Université de Strasbourg, 11 rue de l'Université, 67000 Strasbourg, France

³ NASA Goddard Space Flight Center, Greenbelt, MD 20771, USA

Received 4 May 2012; accepted October 12 2012

ABSTRACT

Context. Spectral analyses of hot, compact stars with NLTE (non-local thermodynamical equilibrium) model-atmosphere techniques allow the precise determination of photospheric parameters such as the effective temperature (T_{eff}), the surface gravity ($\log g$), and the chemical composition. The derived photospheric metal abundances are crucial constraints for stellar evolutionary theory.

Aims. Previous spectral analyses of the exciting star of the nebula A 35, BD–22°3467, were based on He+C+N+O+Si+Fe models only. For our analysis, we use state-of-the-art fully metal-line blanketed NLTE model atmospheres that consider opacities of 23 elements from hydrogen to nickel. We aim to identify all observed lines in the ultraviolet (UV) spectrum of BD–22°3467 and to determine the abundances of the respective species precisely.

Methods. For the analysis of high-resolution and high-S/N (signal-to-noise) FUV (far ultraviolet, *FUSE*) and UV (HST/*STIS*) observations, we combined stellar-atmosphere models and interstellar line-absorption models to fully reproduce the entire observed UV spectrum.

Results. The best agreement with the UV observation of BD–22°3467 is achieved at $T_{\text{eff}} = 80 \pm 10$ kK and $\log g = 7.2 \pm 0.3$. While T_{eff} of previous analyses is verified, $\log g$ is significantly lower. We re-analyzed lines of silicon and iron (1/100 and about solar abundances, respectively) and for the first time in this star identified argon, chromium, manganese, cobalt, and nickel and determined abundances of 12, 70, 35, 150, and 5 times solar, respectively. Our results partially agree with predictions of diffusion models for DA-type white dwarfs. A combination of photospheric and interstellar line-absorption models reproduces more than 90% of the observed absorption features. The stellar mass is $M \approx 0.48 M_{\odot}$.

Conclusions. BD–22°3467 may not have been massive enough to ascend the asymptotic giant branch and may have evolved directly from the extended horizontal branch to the white dwarf state. This would explain why it is not surrounded by a planetary nebula. However, the star, ionizes the ambient interstellar matter, mimicking a planetary nebula.

Key words. Planetary Nebulae: individual: A66 35 – Stars: abundances – Stars: atmospheres – Stars: evolution – Stars: individual: BD–22°3467 – Stars: white dwarfs

1. Introduction

Abell 35 ($\alpha_{2000} = 12^{\text{h}}53^{\text{m}}32^{\text{s}}.79$, $\delta_{2000} = -22^{\circ}52'22''.55$) was discovered by Abell (1955, A55 24) and classified as a planetary nebula (PN). Abell (1966) characterized it (A66 35, henceforth A 35, PN G303.6+40.0) as a homogeneous disk PN with an angular size between $636''$ and $938''$. Figure 1 shows an image of A 35 with very long exposure time. Its size is about $17'$ in east-west and $14'$ in north-south direction. The nebula shape appears to be quite atypical for a PN. The bow-shock structure is surrounded by a symmetric emission area that does not agree with the usual bi-polar or ellipsoidal morphologies.

Grewing & Bianchi (1988) discovered a hot companion to the visible nucleus in the optical, (SAO 181201, Jacoby 1981). They suggested that it is an extremely hot DAO-type¹ white dwarf (WD). A 35, BD–22°3467 (LW Hya) is therefore a re-

solved binary system (Jacoby 1981; De Marco 2009), composed of a WD star of spectral type DAO and a G8 III-IV - type companion (Unruh et al. 2001; Strassmeier 2009). The latter dominates the spectrum at $\lambda \gtrsim 2800 \text{ \AA}$ (Grewing & Bianchi 1988).

Borkowski et al. (1990) explained the PN asymmetry (Fig. 1) as the result of an interaction between the PN and the surrounding interstellar medium (ISM), the observed bow shock (the star is moving with $v = 125$ km/s) being located at the equilibrium sphere of ram pressure of the accelerated PN gas and the stellar wind ram pressure.

A mean (*HIPPARCOS*, *TYCHO-2*, and *UCAC-2* values) proper motion of $\mu_{\alpha} = -60.95 \pm 1.5$ mas/yr and $\mu_{\delta} = -14.63 \pm 1.4$ mas/yr was measured by Kerber et al. (2008) in agreement with *HIPPARCOS* values (HIP 62905, Van Leeuwen 2007) of $\mu_{\alpha} = -60.91 \pm 1.62$ mas/yr $\mu_{\delta} = -13.41 \pm 1.24$ mas/yr. With its high proper motion, BD–22°3467 passes through the complete visible nebula within about 16 000 years (Fig. 1). Recently, Frew & Parker (2010) claimed A 35 to be a “bow shock nebula in a photoionized Strömgren sphere in the ambient ISM”. This scenario does not include a PN. Weidmann & Gamen (2011), however, classified A 35 as a binary PN (? + G8 IV) with a bc-CSPN (corresponding to binarity for the cool CSPN).

* Based on observations with the NASA/ESA Hubble Space Telescope, obtained at the Space Telescope Science Institute, which is operated by the Association of Universities for Research in Astronomy, Inc., under NASA contract NAS5-26666.

** Based on observations made with the NASA-CNES-CSA Far Ultraviolet Spectroscopic Explorer.

¹ spectral classification: characteristic H I and He II absorption lines



Fig. 1. A 35: Narrow-band composite of H α , [O III], and [S II] (in total 36 h exposure time) by Dean Salman (Sh2-313, <http://www.sharplesscatalog.com/>). N is up, E is left, the FOV is 20' \times 20'. The (red) arrow indicates the projected motion of BD-22°3467 during the last 10 000 years.

HIPPARCOS measured a parallax of 7.48 ± 1.55 mas (Perryman et al. 1997, $D = 134^{+35}_{-24}$ pc). This was corrected later by Gatti et al. (1998) to $D = 163^{+96}_{-58}$ pc (this value was adopted by Herald & Bianchi 2002). Gatti et al. (1998) determined a separation of the hot and cool component of 13 – 28 AU at this distance. However, they adopted 160 pc as a minimum distance because previous estimates (see their Table 2) gave much higher values (e.g. 360 ± 80 pc from photometry measured by Jacoby 1981). Van Leeuwen (2007) presented a validation of the new *HIPPARCOS* reduction. The improved parallax (8.38 ± 1.57 mas) is slightly larger with a similar error range. The corresponding distance of $D = 119^{+28}_{-19}$ pc is now even smaller.

Herald & Bianchi (2002) determined the atmospheric parameters of both components and found $T_{\text{eff}} = 80$ kK, $\log g = 7.7$ (cm/s²) for the WD, and $T_{\text{eff}} = 5$ kK, $\log g = 3.5$ for its companion star. Their hot-component analysis of UV spectra (*FUSE*², *HST/STIS*³, and *IUE*⁴) covering $905 \text{ \AA} \lesssim \lambda \lesssim 3280 \text{ \AA}$ was performed with *TLUSTY* and *SYNSPEC* (Hubeny 1988; Hubeny & Lanz 1992, 1995; Hubeny et al. 1994). They determined abundances for He, C, N, O, Si, and Fe (Tab. 4). For the analysis of the cool companion they used LTE (local thermodynamical equilibrium) models (Kurucz 1991).

State-of-the-art NLTE (Non-Local Thermodynamical Equilibrium) model atmospheres are fully metal-line blanketed and can consider all elements from hydrogen to nickel (Rauch 2003; Rauch et al. 2007). Therefore, we decided to re-analyze the available UV spectra of BD-22°3467 to determine abundances of hitherto neglected metals. The resulting abundance pattern can give clues to the evolutionary history of the DAO

star. We begin with a brief description of the observed UV spectra and preparatory work (Sect. 2), followed by an introduction to our model atmospheres (Sect. 3). Then we describe our spectral analysis (Sect. 4) in detail and discuss the results in Sect. 5.

2. Observations and interstellar absorption

Hot post-AGB (asymptotic giant branch) stars have their flux maximum in the UV wavelength range. Most of the exhibited metal lines are located there. Metal lines of successive ionization stages allow one to evaluate the ionization equilibrium of the respective species. This is a very sensitive indicator for T_{eff} . The error ranges of T_{eff} and abundance determinations can be reduced by the analysis of many spectral lines.

The dominant ionization stages of the iron-group elements in the relevant T_{eff} and $\log g$ regime are v and vi (Fig. 2). Many strategic lines of these ions are located in the UV wavelength range. We therefore retrieved *FUSE*, *HST/STIS*, and *IUE* observations from the MAST⁵ archive (Tab. 1).

Our spectral analysis is based on the high-resolution *FUSE* and *STIS* observations. The four *STIS* spectra were co-added to improve the S/N. Herald & Bianchi (2002) analyzed the same *FUSE* spectrum but only one (O4GT02010) of the *STIS* spectra. The low-resolution *IUE*⁶ observations were used in addition to determine the interstellar reddening (E_{B-V} , Fig. 3) as well as to verify the flux calibration. The *STIS* observation had to be scaled by a factor of 1.995 to match the flux level of the *IUE* observation. This offset is possibly due to bad centering of the exciting star during the exposure (Herald & Bianchi 2002).

2.1. Interstellar absorption and reddening

The general procedure of determining the interstellar reddening is to normalize a theoretical spectrum as far as possible in the low-energy range because it is not significant there. In the case of BD-22°3467, the companion star dominates the observation at wavelengths longer than $\approx 2800 \text{ \AA}$. Therefore, we constructed a theoretical, composite spectrum (with appropriate stellar radii, $R_{\text{pri}}^2/R_{\text{s}}^2 = 7.43 \cdot 10^{-5}$) using our final model spectrum ($T_{\text{eff}} = 80$ kK, $\log g = 7.2$) and a Kurucz model⁷ ($T_{\text{eff}} = 5000$ K, $\log g = 3.5$, solar abundances $\log Z = 0.0$) for the hot and cool component, respectively. This spectrum was then normalized to the 2MASS K flux (Fig. 3). The best fit (matching all *GALEX*, *HIPPARCOS*, and 2MASS magnitudes and the UV spectra) was achieved for $E_{B-V} = 0.02 \pm 0.02$, using the reddening law of Fitzpatrick (1999) with the standard $R_v = 3.1$. Our value agrees within error limits with those of Herald & Bianchi (2002, $E_{B-V} = 0.04 \pm 0.01$), who used the Rayleigh-Jeans tail of the UV observations ($1000 \text{ \AA} \lesssim \lambda \lesssim 2800 \text{ \AA}$) only.

To determine the column density of interstellar neutral hydrogen, n_{HI} , models with different n_{HI} were compared with Ly α . We found a best fit for $n_{\text{HI}} = 5.0 \pm 1.5 \times 10^{20} \text{ cm}^{-2}$ (Fig. 4), which agrees with the value found by Herald & Bianchi (2002).

2.2. Radial velocity of the hot component

The *STIS* observation shows numerous sharp, isolated photospheric lines that are suitable to determine v_{rad} . On average (21

² Far Ultraviolet Spectroscopic Explorer

³ Hubble Space Telescope/Space Telescope Imaging Spectrograph

⁴ International Ultraviolet Explorer

⁵ <http://archive.stsci.edu/>

⁶ International Ultraviolet Explorer

⁷ <ftp://ftp.stsci.edu/cdbs/grid/k93models/kp00/>

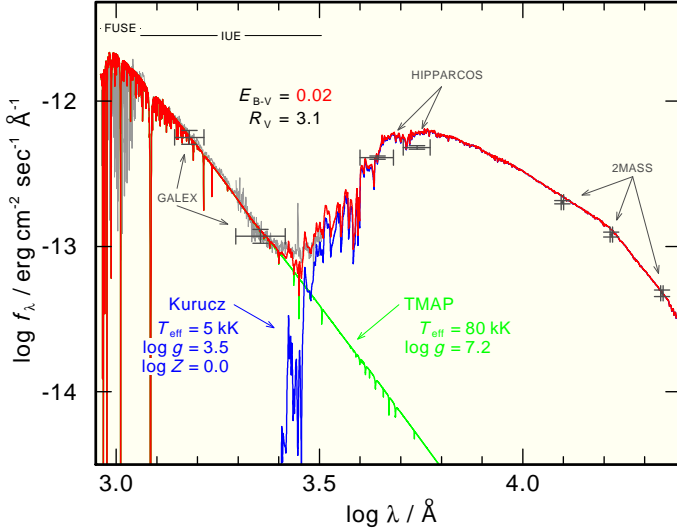


Fig. 3. UV-optical-IR flux distribution of the BD-22°3467 binary system, fitted by atmosphere models for both components.

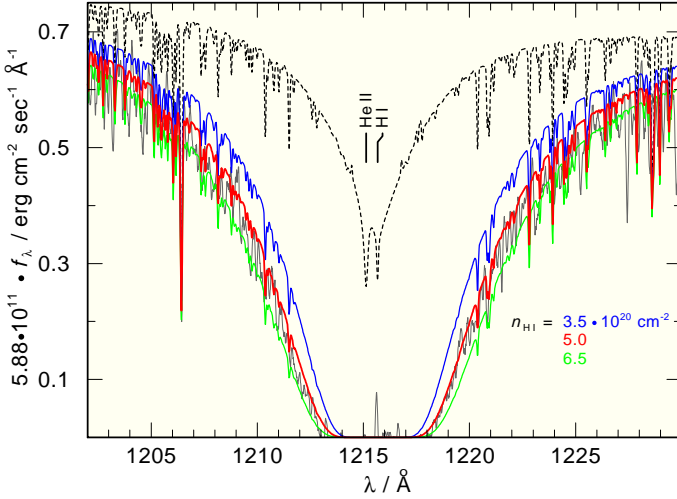


Fig. 4. STIS observation around H I Ly α compared with our final model (Tab. 4) at different $n_{\text{H I}}$. The dashed line is the WD's atmospheric flux.

lines of N v, O iv, O v, Ar v, Cr v, Cr vi, Fe v, Fe vi, and Ni v), we measured $v_{\text{rad}} = -14.4 \pm 0.7 \text{ km sec}^{-1}$.

3. Model atmospheres and atomic data

In this section, we briefly describe the atomic data and the programs used for our analysis. Details about the calculation of the stellar atmosphere models can be found in Sect. 3.1. The usage of *OWENS* for the calculation of the ISM absorption is described in Sect. 3.2.

3.1. The photospheric model for the hot component

Our model atmospheres (plane-parallel, chemically homogeneous, in hydrostatic and radiative equilibrium) are calculated with *TMAP*⁸, the Tübingen NLTE model atmosphere package (Werner et al. 2003). We calculated a small grid of models that include opacities of 23 elements from H – Ni (Tab. 2).

⁸ <http://astro.uni-tuebingen.de/~TMAP>

H – Ar are represented by “classical” model atoms (Rauch 1997) taken from *TMAD*⁹, the Tübingen model atom database. For Ca – Ni, a statistical approach was applied to handle the large number of atomic levels and line transitions. We employed *IrOnIc* (Rauch & Deetjen 2003; Rauch 2003) to consider thousands of levels and millions of lines provided by Kurucz (2009, and priv. comm.) and the Opacity Project (Seaton et al. 1994).

Kurucz’s line lists are divided into so-called LIN (measured and theoretical lines) and POS (only measured, “good” wavelengths) lists. For the model-atmosphere calculations, the LIN lists were used, to consider the total opacity properly. To calculate the emerging spectrum, POS lists were used to identify iron-group lines. Figure 5 demonstrates the difference between LIN and POS line lists. As an example for all species and their ions serves Cr v (within the shown 1470 – 1500 Å interval). At present, Kurucz provides 73 222 LIN and 249 POS lines of Cr v, 459 LIN and 6 POS lines in this wavelength interval. We adjusted the Cr abundance to $[\text{Cr}] = +3.1$ to reproduce the two strongest Cr v POS lines, Cr v $\lambda\lambda$ 1482.76, 1489.71 Å. At this abundance, most of the prominent Cr v LIN lines appear displaced or simply too strong. An exception is Cr v λ 1481.66 Å, which matches the observation well. It can not be excluded that the Cr v λ 1490.24 Å LIN lines in the model is the observed 1490.66 Å line, for instance. However, reliable abundance determinations are only possible using unambiguously identified POS lines (Sect. 4.3).

In the framework of the Virtual Observatory (*VO*¹⁰), all spectral energy distributions (SEDs, $\lambda - F_\lambda$) calculated from our model-atmosphere grid are available in *VO*-compliant form from the registered *VO* service *TheoSSA*¹¹ provided by the *German Astrophysical Virtual Observatory (GAVO)*¹².

3.2. The ISM line-absorption model

In the *FUSE* wavelength range (Fig. 6), numerous interstellar H₂ and H I absorption lines hamper the analysis of the photospheric spectrum. We applied the program *OWENS* to calculate ISM line-absorption models. *OWENS* allows one to model different clouds with distinct radial and turbulent velocities, temperatures, column densities, and chemical compositions. It fits Voigt profiles using a χ^2 minimization. For more information on *OWENS*, see e.g. Hébrard et al. (2002) or Hébrard & Moos (2003).

Figure 6 shows a small section of the *FUSE* spectrum of BD-22°3467. Only the combination of the photospheric and ISM-model spectra reproduces most of its spectral features. Our ISM model includes lines of H I, H₂ ($J = 0 - 9$), HD, C II – IV, N I – III, N v, O I, O VI, Mg II, Al II, Si II – IV, P II, S II – III, S VI, Ar I – II, Mn II, Fe II, and Ni II. The radial velocity of the interstellar low-ionization (I – II) atomic gas and H₂ is found to be $v_{\text{rad}} = 6 \pm 2 \text{ km/s}$.

4. Analysis

In this section, we begin with a verification of those atmospheric parameters that were already determined by Herald & Bianchi (2002) which may deviate because these authors used *TLUSTY* and considered He, C, N, O, Si, and Fe, while we employed

⁹ <http://astro.uni-tuebingen.de/~TMAD>

¹⁰ <http://www.ivoa.net>

¹¹ <http://dc.g-vo.org/theossa>

¹² <http://www.g-vo.org>

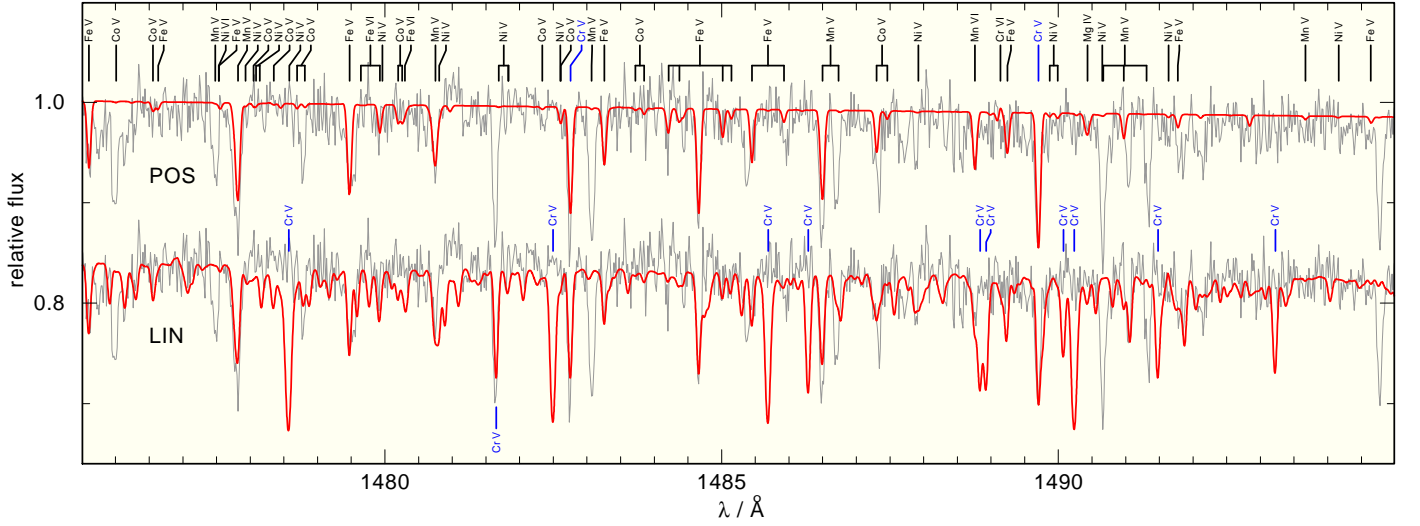


Fig. 5. Section of the *STIS* spectrum (black line) compared with our *TMAP* model. The SED in the upper panel was calculated using Kurucz's POS data (the strongest lines are identified at top), the SED in the lower panel using LIN data. This section contains mainly Fe v - vi and Mn v - vi lines. The strongest Cr v LIN lines are identified at the bottom.

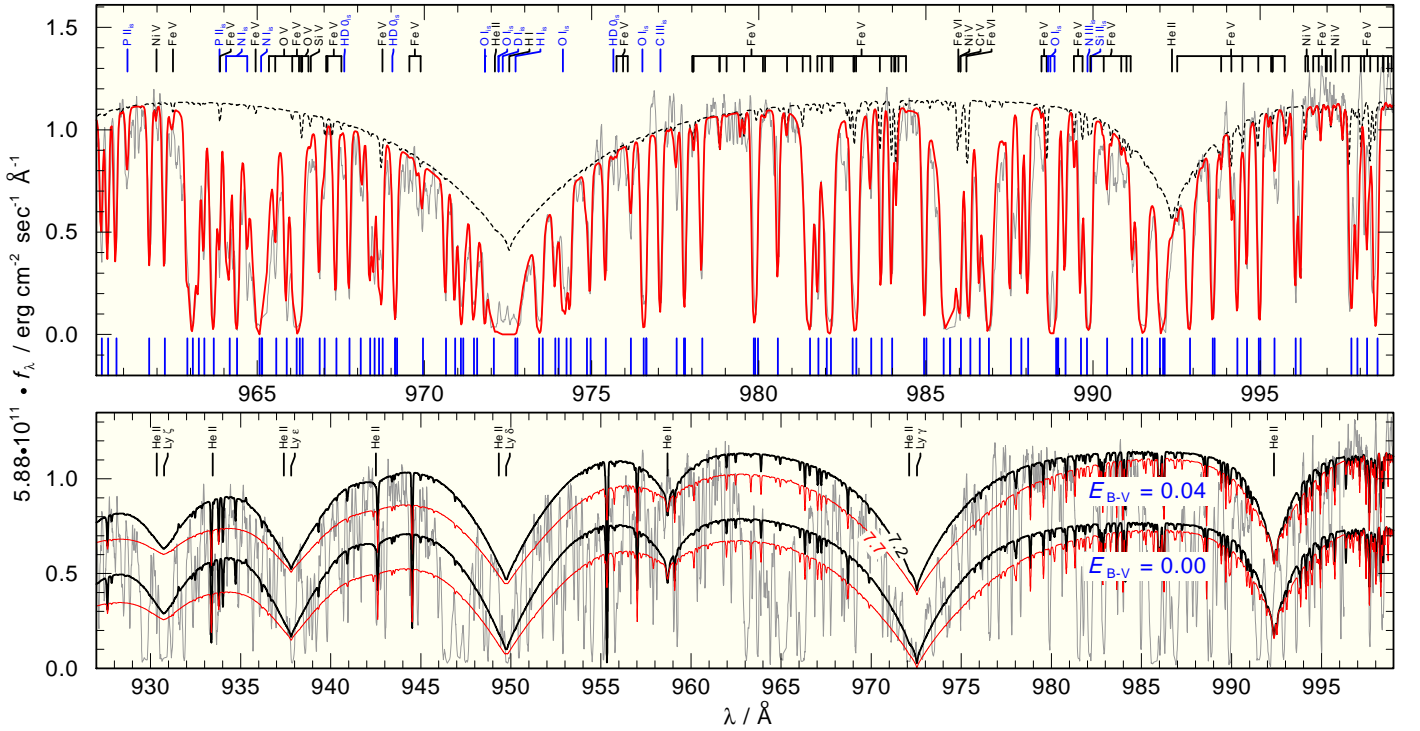


Fig. 6. Top: Section of the *FUSE* observation showing the necessity of a detailed modeling of the ISM. The dashed line is the final, pure photospheric model. The full (red) line shows a combined stellar and interstellar model. Blue marks at the bottom denote interstellar H₂ absorption lines. Bottom: Comparison of (pure photospheric) *TMAP* models with $\log g = 7.2$ (thick, black) and $\log g = 7.7$ (thin, red), normalized to the flux of the $\log g = 7.2$ model at 999 Å for comparison. The full lines are calculated with the determined reddening of $E_{B-V}^{\max} = 0.04$ (Sect. 2.1), the dashed lines (shifted in $\log f_{\lambda}$ by -0.4 for clarity) with $E_{B-V}^{\min} = 0$.

TMAP with far more elements (Tab. 2). This might result in a different atmospheric structure. We begin with models with parameters of Herald & Bianchi (2002) and fine-tune them if necessary.

4.1. Effective temperature and surface gravity

Herald & Bianchi (2002) determined $T_{\text{eff}} = 80$ kK and $\log g = 7.7$. *TMAP* test calculations showed that their T_{eff}

value matches all ionization equilibria well, e.g. N iv/N v, O iv/O v, and Mn v/Mn vi (Sect. 4.3). A lower $\log g = 7.2$ yields a significantly better fit agree of the theoretical He II $\lambda 1640.42$ Å line profile with the observation in the line core, which is not matched at $\log g = 7.7$ (Fig. 7). For the line-profile calculations, we used the Stark line-broadening tables by Schöning & Butler (1989a,b). The line wings are too broad at $\log g = 7.7$ and somewhat too weak at $\log g = 7.2$. The

same is true for He II $\lambda 1084.94 \text{ \AA}$ (Fig. 7). The decrements of spectral line series such as the H I Balmer (Rauch et al. 1998), H I Lyman (transitions $n - n' = 1 - 3$ to $1 - 8$), and He II $2 - n'$ series ($2 - 5$ to $2 - 11$) are strongly dependent on $\log g$. The fit to the outer line wings of the latter two series in the *FUSE* spectrum is also very well reproduced at $\log g = 7.2$. Figure 6 shows He II $2 - 5$ to $2 - 14$ and the respective H I $1 - 3$ to $1 - 7$ blends. A comparison of their theoretical profiles at $\log g = 7.2$ and $\log g = 7.7$ with the observation shows that they are significantly too broad at $\log g = 7.7$. This effect cannot be compensated for by a lower E_{B-V} (Fig. 6). The interstellar H I absorption is not dominating the wings of these lines. The observed “shoulders” between the H I Lyman lines and, thus, the Lyman decrement is well reproduced at $\log g = 7.2$ and is definitely missed at $\log g = 7.7$. This is best visible between Ly ζ and Ly δ because the contamination of the *FUSE* observation with ISM lines is obviously weak. $\log g = 7.2$ agrees with the value of Herald & Bianchi (2002) within *realistic* error limits of 0.3 dex. Their assumed statistical error ($\log g = 7.7^{+0.13}_{-0.18}$) seems to be too optimistic. We finally adopted $T_{\text{eff}} = 80 \pm 10 \text{ kK}$ and $\log g = 7.2 \pm 0.3$ for our analysis.

4.2. Hydrogen and helium

We adopted $[\text{He}] = -0.3$ ($[\text{X}]$ denotes $\log [\text{mass fraction} / \text{solar mass fraction}]$ for species X) from Herald & Bianchi (2002) and achieved a reasonable fit to the He II lines (Fig. 7).

4.3. Metal abundances

In our *TMAP* model-atmosphere calculations, we considered opacities of all elements from H to Ni except for Li, Be, B, Cl, and K. We convolved our synthetic spectra with Gaussians to simulate the respective instrument resolution. By comparison with the observed spectrum of BD-22°3467, we determined for the first time photospheric abundances of Ar, Cr, Mn, Co, and Ni. All identified lines of these species in the available observations (Sect. 2) were evaluated in our abundance analysis. No lines of F, Ne, Na, Mg, Al, Ca, Sc, Ti, and V were identified. For these, only upper limits could be derived by test models where the respective lines in the model emerge (at the abundance limit) from the noise in the observation. A detailed comparison of models with different abundances of individual metals showed that the typical abundance error is ± 0.3 dex. In the following, we briefly describe some measurements (ordered by increasing atomic weight).

Carbon lines of stellar origin are not detectable in the spectrum of BD-22°3467. Narrow interstellar C IV $\lambda\lambda 1548.20, 1550.77 \text{ \AA}$ lines are present (Fig. 8) that virtually “bracket” the photospheric lines ($v_{\text{rad}}^{\text{star}} = -14.4 \text{ km/s}$, Sect. 2.2). They have their origin in two different interstellar “clouds” with different radial velocities and column densities (cloud 1: $v_{\text{rad}} = -5.4 \text{ km/s}$, $\log(n_{\text{CIV}}/(\text{g/cm}^2)) = 16.8$; cloud 2: $v_{\text{rad}} = -30.4 \text{ km/s}$, $\log(n_{\text{CIV}}/(\text{g/cm}^2)) = 14.6$). The radial velocity of cloud 1 agrees with the velocity of the low-ionization ISM gas (Sect. 3.2). Interestingly, Schneider et al. (1983) determined $v_{\text{rad}} = -6.6 \pm 3.8 \text{ km/sec}$ for the nebula. This even suggests a nebular origin of cloud 1 while cloud 2 with its significantly higher velocity lies on the line of sight toward us.

It is worthwhile to note that no other interstellar two-component absorption-line feature is identified in the spectrum of BD-22°3467.

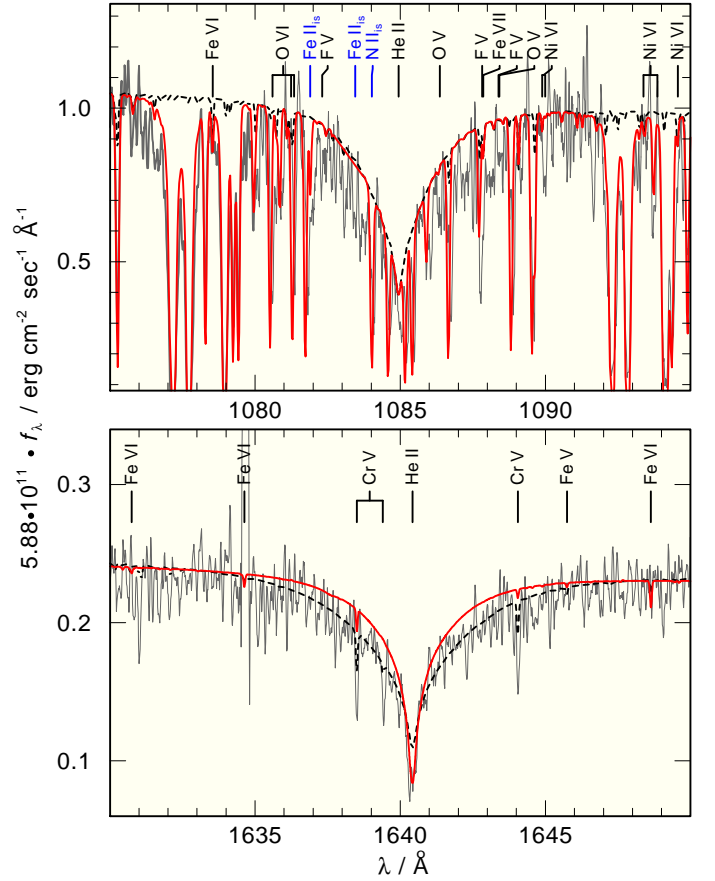


Fig. 7. Spectra of our final model compared with the *FUSE* and *STIS* observations around He II $\lambda 1084.94 \text{ \AA}$ (top, dashed: pure photospheric, full line: photospheric + ISM line absorption) and He II $\lambda 1640.42 \text{ \AA}$ (bottom, dashed: $\log g = 7.7$, full line: $\log g = 7.2$). The identified lines are marked. Most of the very strong absorptions in the top panel stem from H₂.

However, a photospheric component, even at low abundance, worsens the agreement between model and observation in the shoulder between the interstellar lines (Fig. 8). Since the strongest C IV lines in the *FUSE* wavelength range ($\lambda\lambda 948, 1107, 1168 \text{ \AA}$) become too strong for $[\text{C}] > -2.9$, we determine this as an upper limit. This value is about four times lower than that found by Herald & Bianchi (2002).

Nitrogen N IV $\lambda 1718.55 \text{ \AA}$ and N V $\lambda\lambda 1238.82, 1242.80 \text{ \AA}$ are prominent in the *STIS* observation. Our final model reproduces the strengths of these lines and the ionization equilibrium at $[\text{N}] = -1.7$ (Fig. 9) well.

Herald & Bianchi (2002) determined a much lower photospheric N abundance ($< 10^{-3}$ times the solar value) because of strong line wings forming at higher abundances. The reason may be a different approximation by the quadratic Stark effect in *TMAP* and *TLUSTY/SYNSPEC*.

For the line-absorption cross-sections *TMAP* calculates

$$\sigma_{ij}(\nu) = \frac{\sqrt{\pi} e^2}{m_e c} \frac{f_{ij}}{\Delta \nu_D} H(a, \nu) \quad (1)$$

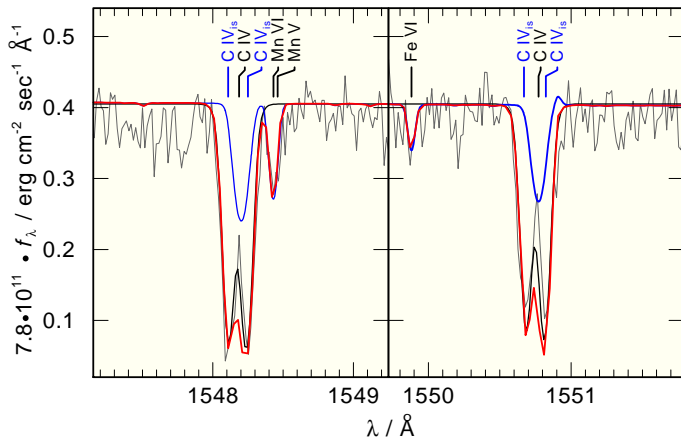


Fig. 8. C IV $\lambda\lambda$ 1548.20, 1550.77 Å lines in the *STIS* observation compared with our final model. Blue, thin: photospheric lines, red, thick: photospheric + interstellar lines, black, thin: interstellar lines.

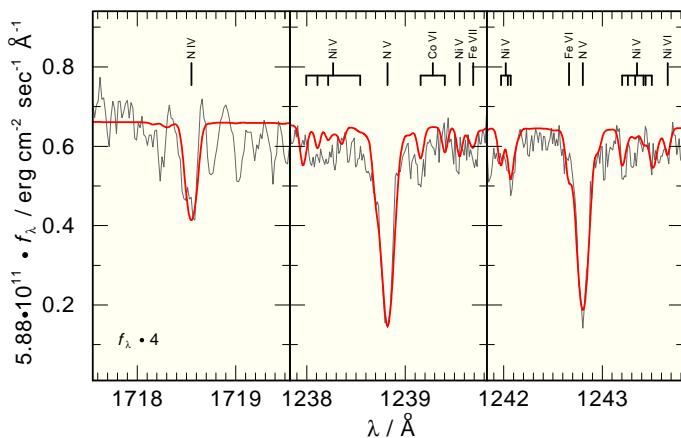


Fig. 9. N IV λ 1718.55 Å and N V $\lambda\lambda$ 1238.82, 1242.80 Å lines in the *STIS* observation compared with our final model.

e and m_e are electron charge and mass, c is the light velocity, $\Delta\nu_D$ the Doppler width, f_{ij} the oscillator strength for the transition $i \rightarrow j$, and H the Voigt function with

$$a = \frac{\Gamma}{4\pi\Delta\nu_D}, \quad (2)$$

and

$$v = \frac{\Delta v}{\Delta v_D}, \quad (3)$$

where $\Delta\nu = \nu - \nu_0$ with the line frequency ν_0 .

According to Cowley (1970, 1971), the line-broadening due to the quadratic Stark effect is approximately given by

$$\Gamma_{Stark} = 5.5 \times 10^{-5} \frac{n_e}{\sqrt{T}} \left[\frac{(n_{\text{eff}}^{\text{up}})^2}{z+1} \right]^2, \quad (4)$$

where n_e is the electron density, T is the temperature, $n_{\text{eff}}^{\text{up}}$ is the effective principal quantum number of the upper level, and z is the effective charge seen by the active electron. Radiative (Γ_{rad}) and collisional damping by electrons is considered so that

$$\Gamma = \Gamma_{\text{rad}} + \Gamma_{\text{Stark}}. \quad (5)$$

TMAP uses f_{ij} of $7.8580 \cdot 10^{-2}$ and $1.5716 \cdot 10^{-1}$, and classical damping constants Γ_{rad} of $1.4401 \cdot 10^{+9}$ and $1.4494 \cdot 10^{+9}$ for N v $\lambda\lambda$ 1242.80, 1238.82 Å, respectively.

A comparison of calculated Γ_{St} values (Sahal-Br  chot priv. comm.) has shown that $\Gamma_{\text{Stark}}^{\text{Cowley}} / \Gamma_{\text{Stark}}^{\text{Sahal-Br  chot}} = 0.33$ is a good approximation for the N v resonance doublet within $10\,000 < T/\text{K} < 200\,000$. We introduced this factor and adopted $\Gamma_{\text{St}} = 3.0 \cdot \Gamma_{\text{Stark}}^{\text{Cowley}}$ for our analysis.

Oxygen is present in the spectra with the ionization stages iv and v. We can reproduce the ionization equilibrium and the line strengths. Figure 10 shows O iv $\lambda\lambda$ 1338.61, 1343.51 Å and O v λ 1371.29 Å at [O] = -2.6. This agrees well with the observation and the value of Herald & Bianchi (2002).

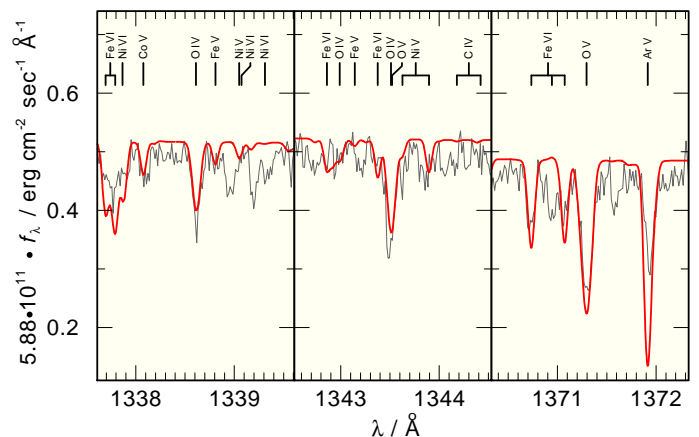


Fig. 10. O IV $\lambda\lambda$ 1338.61, 1343.51 Å (left and middle) and O V λ 1371.29 Å (right) lines in the *STIS* observation compared with our final model.

Fluorine was not identified in the observation. We modeled $F\text{v } \lambda\lambda 1082.31, 1088.38 \text{ \AA}$ and $F\text{VI } \lambda 1139.49 \text{ \AA}$. They would be visible in the observation at abundances higher than solar.

Magnesium lines are weak and almost fade in the noise, even the strongest, $\text{Mg IV } \lambda 1683.003 \text{ \AA}$. Figure 5 shows $\text{Mg IV } \lambda 1490.433 \text{ \AA}$, which is not detectable in the *FUSE* observation at solar abundance. Thus, we can only determine an upper abundance limit of $[\text{Mg}] = 0.0$.

Silicon exhibits only the Si iv $\lambda\lambda$ 1393.76, 1402.77 Å resonance doublet (Fig. 11), other Si lines are too weak. A weak ISM contamination is present but we can determine [Si] = -2.1. This agrees well with the upper limit of Herald & Bianchi (2002).

Argon is strongly enhanced ($[\text{Ar}] = +1.1$). Similar to the central star of the PN Sh 2–216, LS V +46°21 (cf. Rauch et al. 2007), $\text{Ar VI } \lambda\lambda 1283.96, 1303.89, 1307.38 \text{ \AA}$ are identified in the *STIS* observation (Fig. 12) and reproduced by our final model. Our models show a strong $\text{Ar VII } \lambda 1063.55 \text{ \AA}$ line but this is blended by interstellar H_2 absorption and therefore not suitable for a T_{eff} determination via the ionization equilibrium.

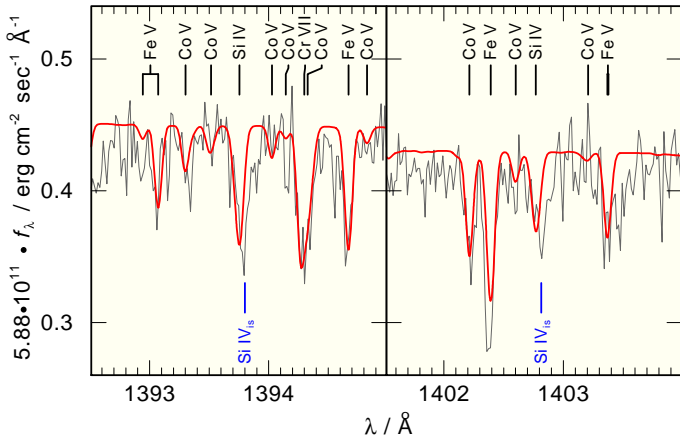


Fig. 11. Si IV $\lambda\lambda$ 1393.76, 1402.77 Å in the *STIS* observation compared with our final model.

A problem are lines like $\text{Ar v } \lambda 1371.92 \text{ \AA}$ (Fig. 10) which are much stronger in our models than observed. Since many ionization equilibria of different species such as $\text{Mn v} - \text{vi}$ (see below) are well-matched, a higher T_{eff} that would shift the ionization balance from Ar v to Ar vi can be excluded. We checked the possibility that the oscillator strengths of Ar v lines that we use in *TMAP* (from the Opacity Project, Seaton et al. 1994) are too strong. The Ar v triplet $3\text{p}^3 \text{ } ^3\text{S}^o - 3\text{p}^4 \text{ } ^3\text{P}$ ($\text{Ar v } \lambda\lambda 1341.57, 1350.39, 1371.92 \text{ \AA}$) is found in OpacityProject data (far off) at 1455.77 \AA (without fine-structure splitting) with $f = 4.2333 \cdot 10^{-2}$. From this value, we calculated f -values of $4.7037 \cdot 10^{-2}$, $1.4111 \cdot 10^{-2}$, and $2.3518 \cdot 10^{-2}$ for the three fine-structure components. A comparison with recent work of Tayal et al. (2009, $f_{1371.92} = 2.257 \cdot 10^{-2}$ and $2.834 \cdot 10^{-2}$) shows good agreement with the OpacityProject. Thus, the reason for the disagreement of the Ar v lines remains unknown.

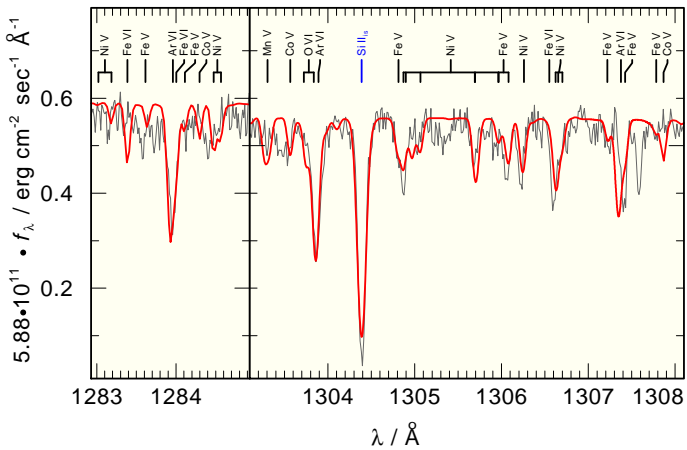


Fig. 12. Section of the *STIS* spectrum around Ar VI $\lambda\lambda$ 1283.96, 1303.89, 1307.38 Å compared with our final, composite photospheric and ISM spectrum.

Chromium is about 70 times enhanced ($[\text{Cr}] = +1.8$). In Fig. 14), $\text{Cr VI } \lambda\lambda 1417.66, 1455.28 \text{ \AA}$ are shown that are well-reproduced by our final model. $\text{Cr V } \lambda\lambda 1482.76, 1489.71 \text{ \AA}$ (Fig. 5) would require a much higher $[\text{Cr}] = +3.1$ (Sect. 3.1). Since T_{eff} and $\log g$ are well-determined (Sect. 4.1) and, thus, a

strong change of the ionization balance toward Cr v is impossible within the error limits, we have to consider these two lines as blends and not suited for a reliable abundance determination.

Manganese exhibits several Mn v and vi lines in the *STIS* wavelength range, e.g. (the strongest) Mn v $\lambda\lambda$ 1359.24, 1382.88, 1432.84, 1440.31, 1443.31, 1452.88, 1457.46, 1480.75, 1486.50 Å and Mn vi $\lambda\lambda$ 1272.44, 1285.10, 1333.87, 1345.49, 1356.85, 1391.17, 1391.22, 1548.43 Å (Fig. 13). All these lines are reproduced at [Mn] = +1.5. Since many lines of two successive ionization stages are suitable for spectral analysis, the Mn v - vi ionization equilibrium is one of the prime indicators for T_{eff} for BD-22°3467. $T_{\text{eff}} = 80$ kK is well-matched at $\log g = 7.2$ (Sect. 4.1).

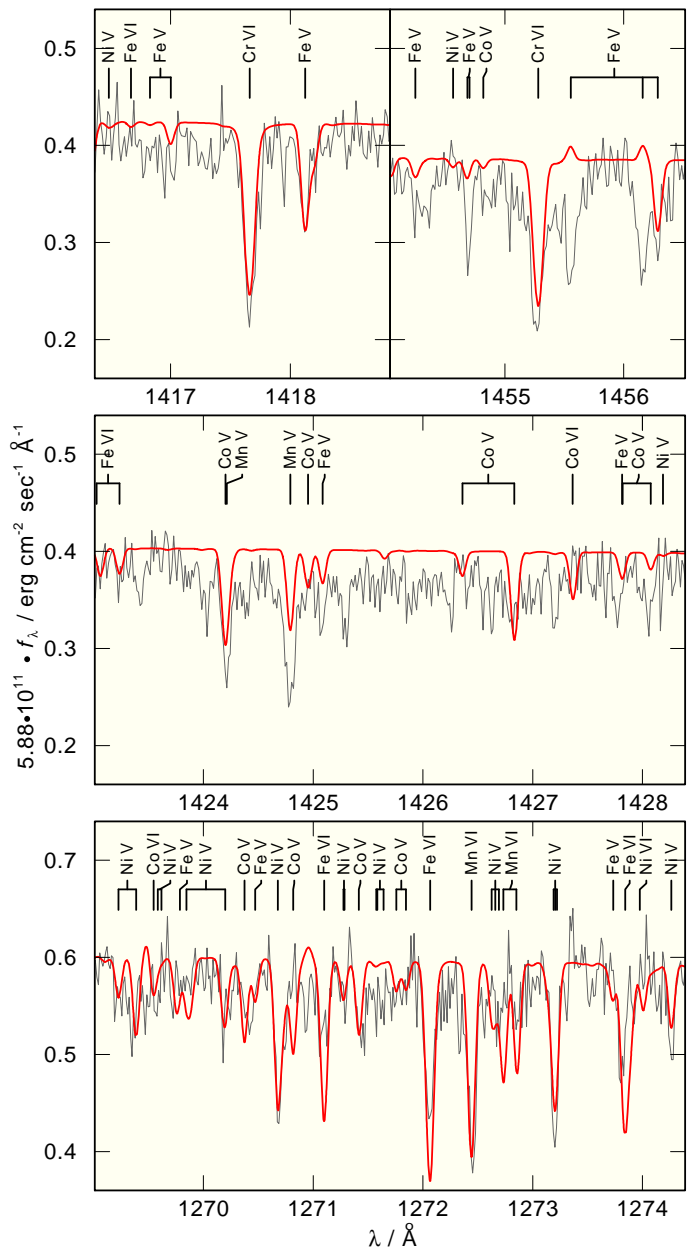


Fig. 14. Sections of the *STIS* observation containing (in addition to others) lines of Cr VI (top), Co (middle), and Ni (bottom) compared with our final model.

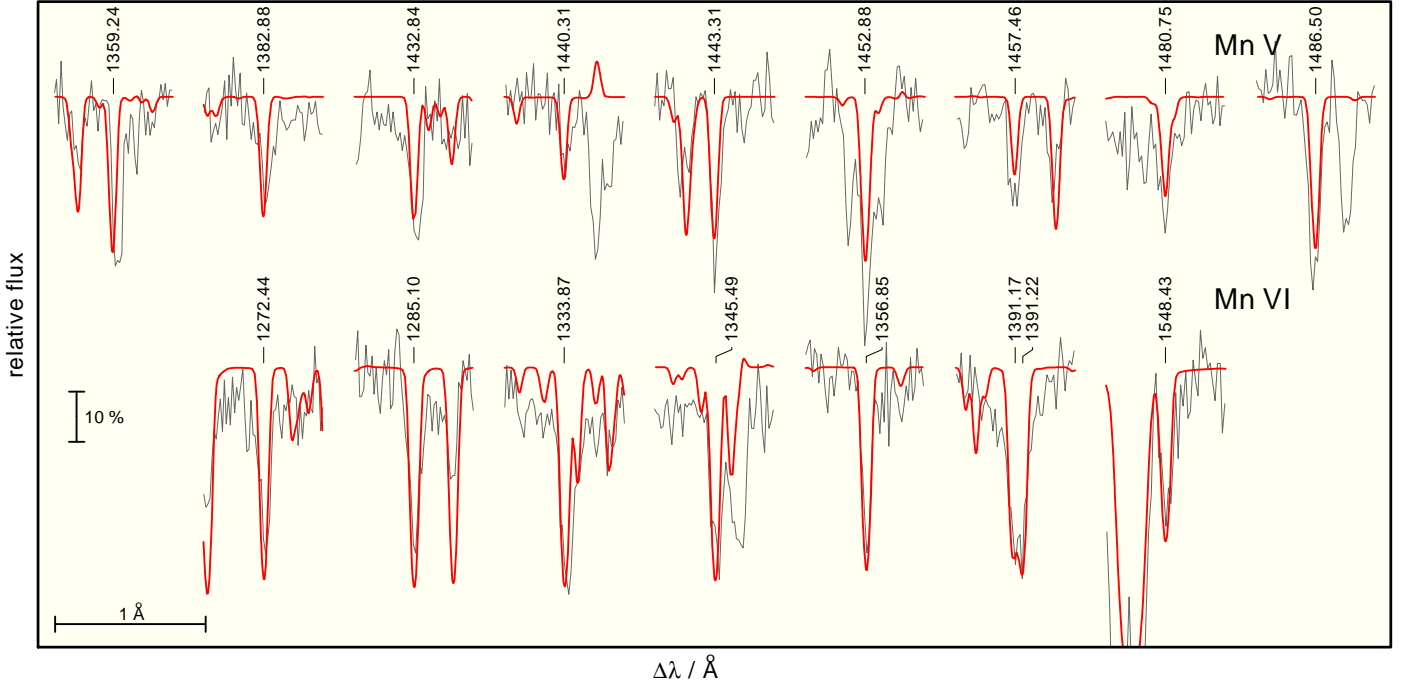


Fig. 13. Strongest Mn v (top) and Mn vi lines (bottom) in the *STIS* wavelength range compared with our final model.

Iron has many lines of Fe v and vi in the UV spectrum. In contrast to Herald & Bianchi (2002), who determined a 0.1 – 0.5 times solar Fe abundance, we find it approximately solar (e.g. Fig. 5). There are, however, some Fe lines that are stronger in our model than observed (see some Fe vi lines in Fig. 14, bottom panel). Within the error range, we find the same Fe abundance as Herald & Bianchi (2002).

Cobalt is strongly enhanced. Co v $\lambda\lambda$ 1331.50, 1349.60 Å indicate [Co] = +2.2 (Fig. 14).

Nickel is also overabundant. Numerous Ni v and vi lines are found in the UV spectrum. They are all reproduced at [Ni] = +0.7 (e.g. Figs. 5, 14).

4.4. Mass, luminosity, radius, and distance

We determined the stellar mass and luminosity from a comparison with evolutionary tracks for hydrogen-rich post-AGB stars (Fig. 15, Miller Bertolami, priv. comm.) and for post-EHB (extended horizontal branch) stars from Dorman et al. (1993, Fig. 17). The results are summarized in Tab. 3.

The stellar radius follows from $R = \sqrt{GM/g}$, where G is the gravitational constant. We determined the spectroscopic distance $D = 361^{+195}_{-137}$ pc (Table 3) following Wassermann et al. (2010). It is derived from

$$D/\text{pc} = 6.6175 \cdot 10^{-6} \sqrt{F_{\nu}/F_{\text{obs}} \cdot M/M_{\odot} \cdot 10^{-\log g}}$$

with the astrophysical flux F_{ν} at the surface of the star as predicted by the model spectrum, and F_{obs} is the observed, extinction-corrected flux (we used $F_{1513\text{Å}}$ to match the center of the *GALEX* FUV band). D is about three times larger than the improved *HIPPARCOS* distance ($D = 119^{+28}_{-19}$ pc, Sect. 1) but it agrees with the photometric distance (360 ± 80 pc, Jacoby 1981) for the cool component.

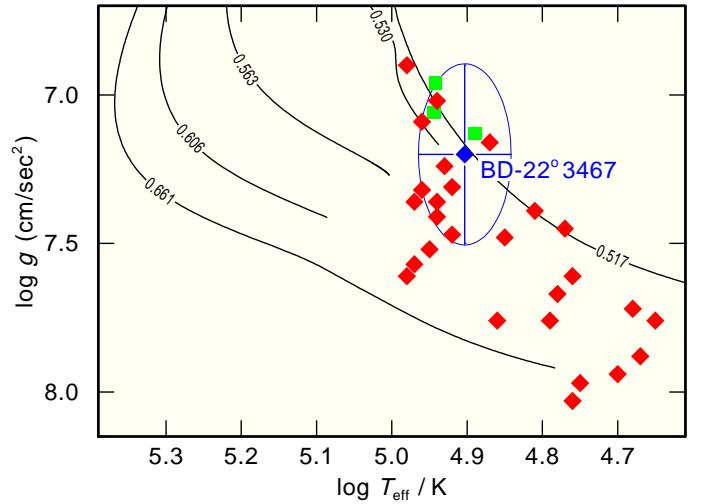


Fig. 15. Location of BD-22°3467 in the $\log T_{\text{eff}} - \log g$ diagram compared with other DAO-type WDs taken from Gianninas et al. (2010, all symbols). Three of these (green squares) are used to compare their metal abundances with those of BD-22°3467 (Fig. 16). The post-AGB evolutionary tracks were calculated by Miller Bertolami (priv. comm.) labeled with the stellar mass (in M_{\odot}).

It is worthwhile to mention that there is no agreement with the *HIPPARCOS* distance at the maximum value of $\log g = 7.83$ given by Herald & Bianchi (2002) either. The calculated spectroscopic distance (using $M = 0.68 M_{\odot}$, $R = 0.017 R_{\odot}$, and the respective model flux) is then $D = 226$ pc, about twice the *HIPPARCOS* distance. Although trigonometric parallaxes in general have to be regarded as hard constraints, orbital movement in binary systems such as BD-22°3467 may bear on the precision of *HIPPARCOS* measurements (cf. Rauch 2000, for LB 3459 = TYC 9166-00716-1). Figures 6 and 7 clearly demonstrate that the spectra cannot be reproduced with a grav-

Table 3. Mass, luminosity, radius, distance, and height above the Galactic plane of BD-22°3467.

	post-AGB evolution	post-EHB evolution
M / M_{\odot}	0.52 ± 0.05	0.48 ± 0.05
$\log L / L_{\odot}$	$1.50^{+0.35}_{-0.45}$	$1.00^{+0.50}_{-0.80}$
R / R_{\odot}	$0.030^{+0.013}_{-0.009}$	$0.029^{+0.012}_{-0.009}$
D / pc	376^{+203}_{-142}	361^{+195}_{-137}
H / pc	233^{+53}_{-66}	224^{+51}_{-62}

ity of $\log g = 7.7$ or higher, while a good fit is achieved for $\log g = 7.2$. The upcoming *GAIA* mission will provide a highly precise parallax for BD-22°3467 which will be able to rule out the uncertainties.

5. Results and discussion

We calculated a grid of *TMAP* NLTE models atmospheres for BD-22°3467, the exciting star of the ionized nebula A 35. We determined $T_{\text{eff}} = 80 \pm 10 \text{ kK}$ and $\log g = 7.2 \pm 0.3$, and thus confirm $T_{\text{eff}} = 80 \text{ kK}$ found by Herald & Bianchi (2002). Nevertheless, we found a somewhat lower $\log g$ than Herald & Bianchi (2002, $\log g = 7.7$). For the first time in this object, abundances from detailed line-profile fits were determined for Ar, Cr, Mn, Co, and Ni (Tab. 4). For F, Ne, Na, Mg, Al, Ca, Sc, Ti, and V, upper limits could be derived.

The element abundance pattern (Fig. 16) is probably the result of the interplay of radiative levitation and gravitational settling. Compared to those objects in the DAO sample from Good et al. (2004, 2005) that have the same T_{eff} and $\log g$ within error limits, BD-22°3467 has a higher He and a lower Si abundance. Cr, Mn, Co, and Ni (not measured by Good et al. 2005) are strongly overabundant, likely due to the force of the radiation field. Radiative levitation may be a reason but the question remains why Fe is about solar. Detailed diffusion calculations that consider these elements are highly desirable investigating this phenomenon. A comparison with existing diffusion calculations (Chayer et al. 1995a,b, Fig. 16) shows (within error limits) that the metal abundances partially agree with predictions for DA-type WDs. Only N, Mg, S, and Ca are more than one dex lower than predicted.

Until recently, BD-22°3467 was believed to be the central star of a planetary nebula and, thus, a post-AGB evolution of an intermediate-mass star ($0.8 M_{\odot} \lesssim M_{\text{initial}} \lesssim 8.0 M_{\odot}$) appeared to be a matter of course. Frew & Parker (2010) showed that the visible, PN-like nebula may be a combination of shock excitation and photoionization of the ambient interstellar gas.

BD-22°3467 provides enough high-energy photons, ($4.4 \cdot 10^{25} \text{ photons/s/cm}^2$ at energies $> 13.6 \text{ eV}$ and $6.4 \cdot 10^{22} \text{ photons/s/cm}^2$ at energies $> 54 \text{ eV}$ calculated from our final model which give totals of $N_{13} = 2.3 \cdot 10^{45} \text{ photons/s}$ and $N_{54} = 3.3 \cdot 10^{42} \text{ photons/s}$, respectively) to ionize the surrounding interstellar gas (cf. Rauch et al. 2004). For $N_{54}/N_{13} < 0.01$, no He II emission from the nebula can be expected. If we assume an electron temperature of $T_e = 10000 \text{ K}$ in the nebula, negligible extinction, $d = 361 \text{ pc}$ (Table 4), and an average angular diameter of $750''$, we derive that BD-22°3467 has a Strömgren sphere with a density of 16 cm^{-3} , $\log(F_{\text{H}\beta}/\text{erg/s/cm}^2) = -11.23$, and an ionized nebular mass of $0.5 M_{\odot}$. The absolute H β flux agrees very well with the value given by Acker et al. (1992, $\log F_{\text{H}\beta} = -11.3$).

Table 4. Results of this work compared with Herald & Bianchi (2002), whose He abundance we adopted.

		this work	H & B
	NLTE code	<i>TMAP</i>	<i>TLUSTY</i>
<i>primary</i>	$T_{\text{eff}} / \text{kK}$	80 ± 10	80 ± 3
	$\log g$	7.2 ± 0.3	$7.7^{+0.13}_{-0.18}$
	$X_{\text{He}}(X_{\odot})$	0.47	$0.3 - 0.5$
	$X_{\text{C}}(X_{\odot})$	1.2×10^{-3}	$5.0 \times 10^{-3} - 10^{-2}$
	$X_{\text{N}}(X_{\odot})$	1.8×10^{-2}	$< 10^{-3}$
	$X_{\text{O}}(X_{\odot})$	2.5×10^{-3}	$5.0 \times 10^{-3} - 10^{-2}$
	$X_{\text{F}}(X_{\odot})$	$\lesssim 1$	
	$X_{\text{Ne}}(X_{\odot})$	< 1	
	$X_{\text{Na}}(X_{\odot})$	< 1	
	$X_{\text{Mg}}(X_{\odot})$	< 1	
	$X_{\text{Al}}(X_{\odot})$	< 1	
	$X_{\text{Si}}(X_{\odot})$	7.5×10^{-3}	$< 10^{-2}$
	$X_{\text{P}}(X_{\odot})$	$< 1.4 \times 10^{-3}$	
	$X_{\text{S}}(X_{\odot})$	$< 1.2 \times 10^{-3}$	
	$X_{\text{Ar}}(X_{\odot})$	12	
	$X_{\text{Ca}}(X_{\odot})$	< 1	
	$X_{\text{Sc}}(X_{\odot})$	< 1	
	$X_{\text{Ti}}(X_{\odot})$	< 1	
	$X_{\text{V}}(X_{\odot})$	< 1	
	$X_{\text{Cr}}(X_{\odot})$	70	
	$X_{\text{Mn}}(X_{\odot})$	35	
	$X_{\text{Fe}}(X_{\odot})$	1	$0.1 - 0.5$
	$X_{\text{Co}}(X_{\odot})$	150	
	$X_{\text{Ni}}(X_{\odot})$	5	
	$E_{\text{B-V}}$	0.02 ± 0.02	0.04 ± 0.01
	$\log n_{\text{H I}}$	20.7 ± 0.1	20.9 ± 0.1
	D^a / pc	361^{+195}_{-137}	163 (<i>HIPPARCOS</i>)
	M^a / M_{\odot}	0.48 ± 0.05	$0.5^{+0.5}_{-0.4}$
	R^a / R_{\odot}	$0.029^{+0.012}_{-0.009}$	$0.0165^{+0.01}_{-0.006}$
	$R^a / D^a / R_{\odot} / \text{kpc}$	$0.080^{+0.004}_{-0.001}$	0.1 ± 0.01
	$\log L^a / L_{\odot}$	$1.00^{+0.50}_{-0.80}$	1.0 ± 0.4
<i>secondary</i>	$T_{\text{eff}} / \text{kK}$	5	5
	$\log g$	3.5	3.5

^a our values for post-EHB evolution

The nebular spectrum by Acker & Stenholm obtained for the catalog (Acker et al. 1992) is weak and, consequently, the $F_{\text{H}\alpha}/F_{\text{H}\beta}$ ratio is overestimated, and the derived extinction of $c = 0.7$ is very uncertain. $F_{[\text{O III}]\lambda 5007 \text{ \AA}}/F_{\text{H}\beta} = 2$ indicates low excitation. Both N II $\lambda\lambda 6548, 6584 \text{ \AA}$ are visible and, with standard assumptions for the nebula but without any correction for unseen higher ionization stages of nitrogen, its nebular abundance may be estimated to be $12 + \log N/H = 7.7$. The Si II $\lambda 6716 \text{ \AA} / \text{Si II } \lambda 6731 \text{ \AA}$ line intensity ratio is at the low-density limit and we can conclude that the nebular electron density is $n_e < 100 \text{ cm}^{-3}$. In addition, we may estimate that the nebular oxygen and sulfur abundances are 7.9 and 6.4, respectively. It is worthwhile to note that the ionized mass of $0.5 M_{\odot}$ is of about the value usually assumed for the average PN mass of $0.2 - 0.3 M_{\odot}$. The reason is simply the fairly low luminosity of BD-22°3467. Such a low-luminosity ionizing star makes a Strömgren sphere that may well mimic a genuine PN. It is thus possible that similar objects have been misclassified as PNe.

Because the time since its departure from the AGB is relatively long for BD-22°3467 due to its low mass (Tab. 3), all matter ejected previously on the AGB (as well as the PN)

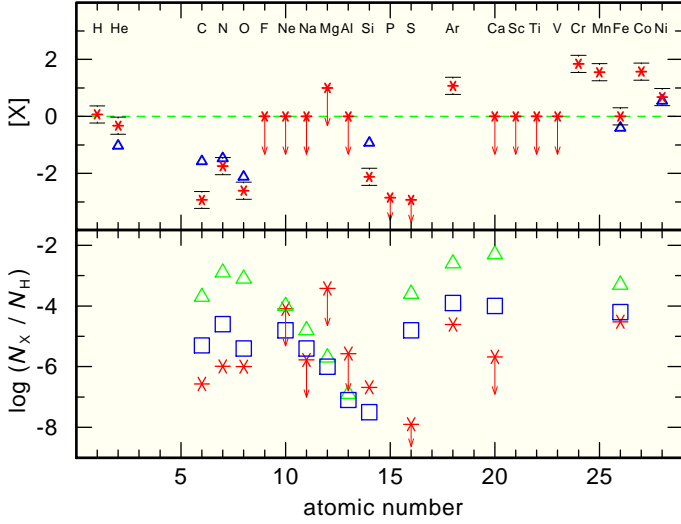


Fig. 16. Top: Photospheric abundances of BD-22°3467 compared with solar values (Asplund et al. 2009), and mean values from three objects of Good et al. (2005, blue triangles) that are located within the error ellipse (cf. Fig. 15, green squares there). Arrows indicate upper limits. Bottom: Comparison of number ratios compared with predictions of diffusion calculations for hydrogen-rich (DA-, blue squares) and helium-rich (DO-type, green triangles) WDs (Chayer et al. 1995a,b) with $T_{\text{eff}} = 80$ kK and $\log g = 7.2$.

may have dissipated into the ambient ISM. Thus, the result of Frew & Parker (2010) does not stringently exclude a post-AGB evolution. However, an alternative stellar evolution may be possible. Bergeron et al. (1994) discussed that the progenitors of most DAO-type WDs are post-EHB stars ($M \approx 0.48 M_{\odot}$). Recently, Gianninas et al. (2010) presented a spectral analysis of 29 DAO- and 18 hot DA-type WDs and found that their DAOs (Fig. 15) are hotter and more massive than previously determined. Accordingly, they concluded that most of these (“a rather mixed bag of objects”) are products of post-AGB evolution. BD-22°3467 is located amongst the low-mass stars of their sample (Fig. 17) and consequently, a post-EHB evolution cannot be ruled out. In this scenario, the stars evolve directly from the EHB to the WD state (AGB-manqué stars, Greggio & Renzini 1990). Bergeron et al. (1994) proposed that a weak mass-loss may keep enough helium in the line-forming regions (Unglaub & Bues 1998, 2000) to exhibit strong He II absorption lines. Figure 17 shows BD-22°3467 in comparison to post-EHB evolutionary tracks (Dorman et al. 1993). One can estimate that an $M \approx 0.48 M_{\odot}$ track (with solar helium content on the horizontal branch, HB) will match the position of BD-22°3467. (Dorman’s tracks for masses higher than $> 0.475 M_{\odot}$ and solar helium content are not fully calculated down to lower T_{eff} and higher $\log g$.) On its way from the EHB to its present position, i.e., towards higher T_{eff} and higher $\log g$, gravitational settling, radiative levitation, and a weak wind are interacting and, thus, the atmospheric abundances may deviate from the HB abundances.

Acknowledgements. MZ was supported by the German Research Foundation (DFG, grant WE1312/38-1). TR is supported by the German Aerospace Center (DLR, grant 05 OR 0806). This research has made use of the SIMBAD database, operated at CDS, Strasbourg, France. This research has made use of NASA’s Astrophysics Data System. This work used the profile-fitting procedure *OWENS* developed by M. Lemoine and the *FUSE* French Team. Some of the data presented in this paper were obtained from the Mikulski Archive for Space

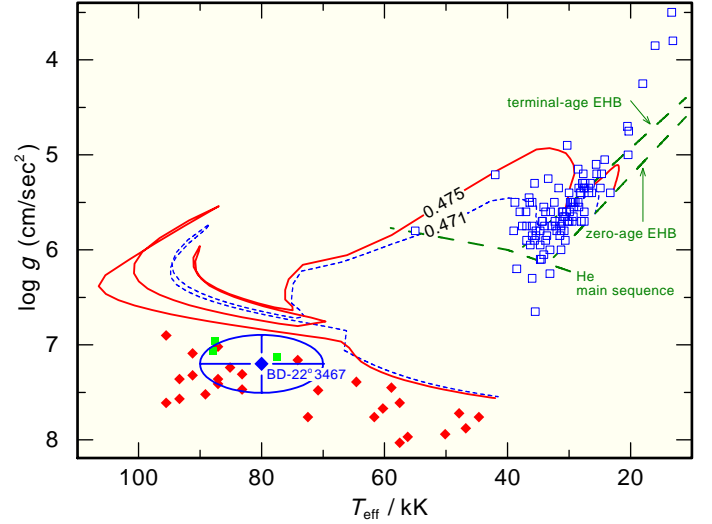


Fig. 17. Location of BD-22°3467 in the $T_{\text{eff}} - \log g$ diagram compared with sd(O)B-type stars close to the EHB taken from Edelmann (blue, open squares 2003) and DAO-type WDs taken from Gianninas et al. (red diamonds and green, filled squares 2010, cf. Fig. 15). The post-EHB evolutionary tracks are from Dorman et al. (1993, $Y = 0.288 \approx Y_{\odot}$) and labeled with the stellar mass (in M_{\odot}).

Telescopes (MAST). STScI is operated by the Association of Universities for Research in Astronomy, Inc., under NASA contract NAS5-26555. Support for MAST for non-HST data is provided by the NASA Office of Space Science via grant NNX09AF08G and by other grants and contracts.

References

- Abell, G. O. 1955, *PASP*, 67, 258
- Abell, G. O. 1966, *ApJ*, 144, 259
- Acker, A., Marcout, J., Ochsenbein, F., et al. 1992, *The Strasbourg-ESO Catalogue of Galactic Planetary Nebulae. Parts I, II*.
- Asplund, M., Grevesse, N., Sauval, A. J., & Scott, P. 2009, *ARA&A*, 47, 481
- Bergeron, P., Wesemael, F., Beauchamp, A., et al. 1994, *ApJ*, 432, 305
- Borkowski, K. J., Sarazin, C. L., & Soker, N. 1990, *ApJ*, 360, 173
- Chayer, P., Fontaine, G., & Wesemael, F. 1995b, *ApJS*, 99, 189
- Chayer, P., Vennes, S., Pradhan, A. K., et al. 1995a, *ApJ*, 454, 429
- Cowley, C. R. 1970, *The theory of stellar spectra* (Gordon & Breach (New York))
- Cowley, C. R. 1971, *The Observatory*, 91, 139
- De Marco, O. 2009, *PASP*, 121, 316
- Dorman, B., Rood, R. T., & O’Connell, R. W. 1993, *ApJ*, 419, 596
- Edelmann, H. 2003, *Dissertation*, University of Erlangen-Nuremberg
- Fitzpatrick, E. L. 1999, *PASP*, 111, 63
- Frew, D. J. & Parker, Q. A. 2010, *PASA*, 27, 129
- Gatti, A. A., Drew, J. E., Oudmaijer, R. D., Marsh, T. R., & Lynas-Gray, A. E. 1998, *MNRAS*, 301, L33
- Gianninas, A., Bergeron, P., Dupuis, J., & Ruiz, M. T. 2010, *ApJ*, 720, 581
- Good, S. A., Barstow, M. A., Burleigh, M. R., et al. 2005, *MNRAS*, 363, 183
- Good, S. A., Barstow, M. A., Holberg, J. B., et al. 2004, *MNRAS*, 355, 1031
- Greggio, L. & Renzini, A. 1990, *ApJ*, 364, 35
- Grewing, M. & Bianchi, L. 1988, in *ESA Special Publication*, Vol. 281, *ESA Special Publication*, 177–178
- Hébrard, G., Friedman, S. D., Kruk, J. W., et al. 2002, *Planet. Space Sci.*, 50, 1169
- Hébrard, G. & Moos, H. W. 2003, *ApJ*, 599, 297
- Herald, J. E. & Bianchi, L. 2002, *ApJ*, 580, 434
- Hubeny, I. 1988, *Computer Physics Communications*, 52, 103
- Hubeny, I., Hummer, D. G., & Lanz, T. 1994, *A&A*, 282, 151
- Hubeny, I. & Lanz, T. 1992, *A&A*, 262, 501
- Hubeny, I. & Lanz, T. 1995, *ApJ*, 439, 875
- Jacoby, G. H. 1981, *ApJ*, 244, 903
- Kerber, F., Mignani, R. P., Smart, R. L., & Wicenc, A. 2008, *A&A*, 479, 155
- Kurucz, R. L. 1991, in *NATO ASIC Proc. 341: Stellar Atmospheres - Beyond Classical Models*, ed. L. Crivellari, I. Hubeny, & D. G. Hummer, 441

- Kurucz, R. L. 2009, in American Institute of Physics Conference Series, Vol. 1171, American Institute of Physics Conference Series, ed. I. Hubeny, J. M. Stone, K. MacGregor, & K. Werner, 43–51
- Perryman, M. A. C., Lindegren, L., Kovalevsky, J., et al. 1997, *A&A*, 323, L49
- Rauch, T. 1997, *A&A*, 320, 237
- Rauch, T. 2000, *A&A*, 356, 665
- Rauch, T. 2003, *A&A*, 403, 709
- Rauch, T. & Deetjen, J. L. 2003, in Astronomical Society of the Pacific Conference Series, Vol. 288, Stellar Atmosphere Modeling, ed. I. Hubeny, D. Mihalas, & K. Werner, 103
- Rauch, T., Dreizler, S., & Wolff, B. 1998, *A&A*, 338, 651
- Rauch, T., Kerber, F., & Pauli, E.-M. 2004, *A&A*, 417, 647
- Rauch, T., Ziegler, M., Werner, K., et al. 2007, *A&A*, 470, 317
- Schneider, S. E., Terzian, Y., Purgathofer, A., & Perinotto, M. 1983, *ApJS*, 52, 399
- Schöning, T. & Butler, K. 1989a, *A&AS*, 79, 153
- Schöning, T. & Butler, K. 1989b, *A&AS*, 78, 51
- Seaton, M. J., Yan, Y., Mihalas, D., & Pradhan, A. K. 1994, *MNRAS*, 266, 805
- Strassmeier, K. G. 2009, *A&A Rev.*, 17, 251
- Tayal, V., Gupta, G. P., & Tripathi, A. N. 2009, *Indian Journal of Physics*, 83, 1271
- Unglaub, K. & Bues, I. 1998, *A&A*, 338, 75
- Unglaub, K. & Bues, I. 2000, *A&A*, 359, 1042
- Unruh, Y. C., Gatti, A. A., Drew, J. E., et al. 2001, in Astronomical Society of the Pacific Conference Series, Vol. 223, 11th Cambridge Workshop on Cool Stars, Stellar Systems and the Sun, ed. R. J. Garcia Lopez, R. Rebol, & M. R. Zapaterio Osorio, 1320
- Van Leeuwen, F. 2007, *A&A*, 474, 653
- Wassermann, D., Werner, K., Rauch, T., & Kruk, J. W. 2010, *A&A*, 524, A9
- Weidmann, W. A. & Gamen, R. 2011, *A&A*, 526, A6
- Werner, K., Deetjen, J. L., Dreizler, S., et al. 2003, in Astronomical Society of the Pacific Conference Series, Vol. 288, Stellar Atmosphere Modeling, ed. I. Hubeny, D. Mihalas, & K. Werner, 31

Table 1. Log of the UV observations of BD–22°3467. The *FUSE* observation was performed with the LWRs (low-resolution aperture, resolving power $R = \lambda/\Delta\lambda \approx 20\,000$), *STIS* with grating E140M ($R \approx 45\,800$), and *IUE* in low-resolution mode ($R \approx 300$).

Instrument	ObsId	Start time (UT)	Exp. time (s)
<i>FUSE</i>	P1330101000	2000-05-20 20:27:37	4 416
<i>STIS</i>	O4GT02010	1999-04-17 21:14:49	2 050
	O4GT02020	1999-04-17 22:37:03	2 800
	O4GT02030	1999-04-18 00:16:10	2 740
	O4GT02040	1999-04-18 01:52:54	2 740
<i>IUE</i>	SWP44121LL	1992-03-06 04:50:23	1 440
	LWP22518LL	1992-03-06 05:26:54	1 440

Table 2. Statistics of H – Ar model atoms used in our calculations

ion	levels			ion	levels		
	NLTE	LTE	lines		NLTE	LTE	lines
H I	12	4	66	Na VI	43	10	130
H II	1	0	–	Na VII	1	0	0
He I	5	98	3	Mg III	1	34	0
He II	16	16	120	Mg IV	31	0	93
He III	1	0	–	Mg V	15	37	18
C III	6	61	12	Mg VI	1	0	0
C IV	54	4	295	Al III	1	6	0
C V	1	0	0	Al IV	15	2	0
N III	1	65	0	Al V	1	16	0
N IV	16	78	30	Al VI	14	24	16
N V	54	8	297	Al VII	1	0	0
N VI	1	0	0	Si III	3	31	1
O III	3	69	0	Si IV	16	7	44
O IV	18	67	39	Si V	25	0	59
O V	90	36	610	Si VI	1	0	0
O VI	54	8	291	P III	1	9	0
O VII	1	0	0	P IV	15	36	9
F III	1	6	0	P V	18	7	12
F IV	1	10	0	P VI	1	0	0
F V	15	91	31	S IV	6	94	4
F VI	12	115	16	S V	21	89	37
F VII	1	0	0	S VI	18	19	48
Ne II	1	33	0	S VII	1	0	0
Ne III	3	43	0	Ar IV	1	349	0
Ne IV	3	37	0	Ar V	32	329	38
Ne V	20	74	35	Ar VI	16	168	21
Ne VI	1	0	0	Ar VII	40	112	130
Na III	1	186	0	Ar VIII	1	0	0
Na IV	1	237	0				
Na V	8	42	9	total	741	2837	2514

Table 2. Continued for Ca – Ni. The so-called “sample lines” are combined to “super lines” by IrOnIc.

ion	super levels	super lines	sample lines
Ca IV	6	16	20 291
Ca V	6	21	141 956
Ca VI	6	19	114 545
Ca VII	6	21	7 1608
Ca VIII	6	20	9 124
Ca IX	1	0	0
Sc IV	6	20	15 024
Sc V	6	21	261 235
Sc VI	6	19	237 271
Sc VII	6	20	176 143
Sc VIII	6	21	91 935
Sc IX	1	0	0
Ti IV	6	19	1 000
Ti V	6	20	26 654
Ti VI	6	19	95 448
Ti VII	6	20	230 618
Ti VIII	6	21	182 699
Ti IX	1	0	0
V IV	6	19	3 7130
V V	6	20	2 123
V VI	6	19	35 251
V VII	6	19	112 883
V VIII	6	20	345 089
V IX	1	0	0
Cr IV	6	20	234 170
Cr V	6	20	43 860
Cr VI	6	20	4 406
Cr VII	6	19	37 070
Cr VIII	6	20	132 221
Cr IX	1	0	0
Mn IV	6	20	719 387
Mn V	6	20	285 376
Mn VI	6	20	70 116
Mn VII	6	20	8 277
Mn VIII	6	20	37 168
Mn IX	1	0	0
Fe IV	6	20	3 102 371
Fe V	6	20	3 266 247
Fe VI	6	20	991 935
Fe VII	6	20	200 455
Fe VIII	6	18	19 587
Fe IX	1	0	0
Co IV	6	20	552 916
Co V	6	20	1 469 717
Co VI	6	18	898 484
Co VII	6	19	492 913
Co VIII	6	20	88 548
Co IX	1	0	0
Ni IV	6	20	2 512 561
Ni V	6	20	2 766 664
Ni VI	6	18	7 408 657
Ni VII	6	18	4 195 381
Ni VIII	6	20	1 473 122
Ni IX	1	0	0
total	279	884	33 219 636

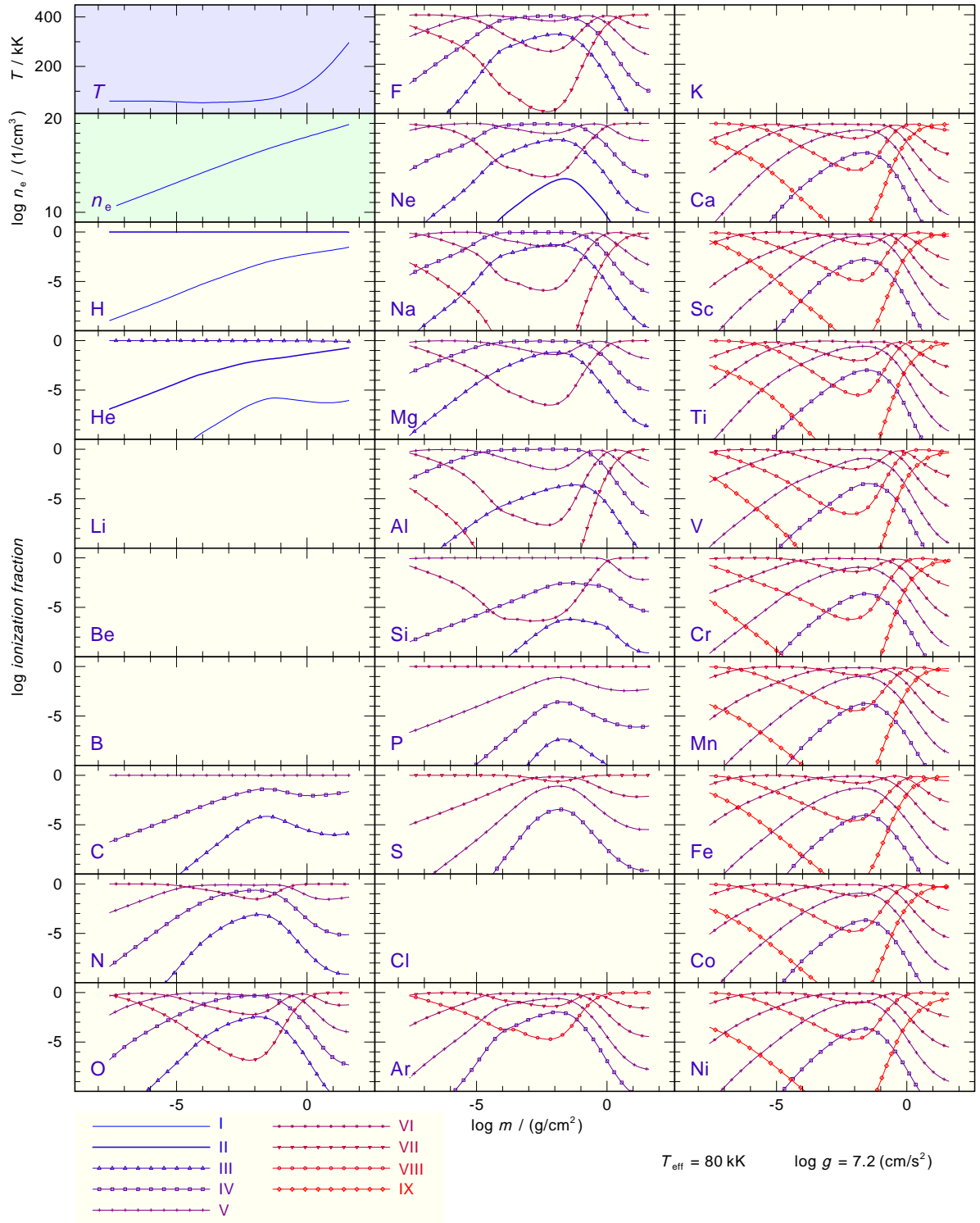


Fig. 2. Temperature and electron density stratification along with ionization fractions of all elements in our final model.